Volume 13
Number 29
7 August 2022
Pages 8447–8706

Chemical Science

rsc.li/chemical-science

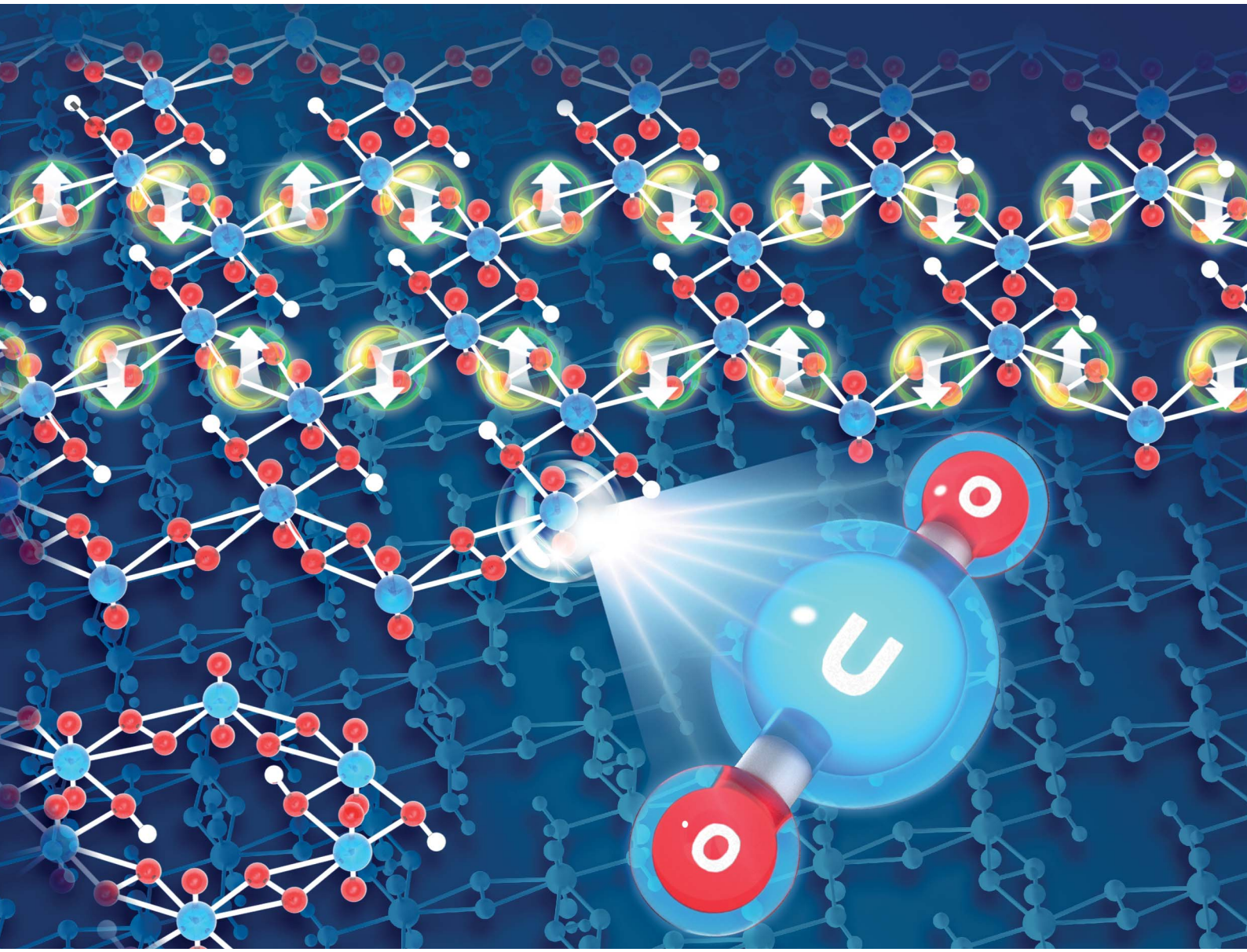

ISSN 2041-6539

ROYAL SOCIETY OF CHEMISTRY

EDGE ARTICLE

Han-Shi Hu *et al.*

Theoretical prediction of a graphene-like 2D uranyl material with p-orbital antiferromagnetism

Chemical Science

ROYAL SOCIETY OF CHEMISTRY

EDGE ARTICLE

View Article Online
View Journal | View Issue

Cite this: *Chem. Sci.*, 2022, **13**, 8518

All publication charges for this article have been paid for by the Royal Society of Chemistry

Received 8th April 2022
Accepted 23rd May 2022

DOI: 10.1039/d2sc02017c

rsc.li/chemical-science

Theoretical prediction of a graphene-like 2D uranyl material with p-orbital antiferromagnetism†‡

Xiao-Kun Zhao, [a] Chang-Su Cao, [a] Jin-Cheng Liu,[a] Jun-Bo Lu,[b] Jun Li [ab] and Han-Shi Hu *[a]

Versatile graphene-like two-dimensional materials with s-, p- and d-block elements have aroused significant interest because of their extensive applications while there is a lack of such materials with f-block elements. Herein we report a unique one composed of the f-block element moiety of uranyl (UO_2^{2+}) through a global-minimum structure search. Its geometry is found to be similar to that of graphene with a honeycomb-like hexagonal unit composed of six uranyl ligands, where each uranyl is bridged by two superoxido groups and a pair of hydroxyl ligands. All the uranium and bridging oxygen atoms form an extended planar 2D structure, which shows thermodynamic, kinetic and thermal stabilities due to σ/π bonding as well as electrostatic interactions between ligands. Each superoxido ligand has one unpaired $(2p_{\pi^*})^1$ electron and is antiferromagnetically coupled through uranyl bridges with $2p_{\pi^*}$–$5f_\delta$–$2p_{\pi^*}$ superexchange interactions, forming a rare type of one-dimensional Heisenberg chain with p-orbital antiferromagnetism, which might become valuable for application in antiferromagnetic spintronics.

Introduction

Two-dimensional (2D) materials have versatile applications in physics, chemistry, and materials science.[1–12] There has been an exponential increase in 2D material research since the isolation of single-layer graphene by Novoselov and Geim in 2004 due to its promising mechanical, superconducting, optical, and chemical properties.[13–16] Currently, a number of graphene-like materials from various types of elements are known, such as 2D ionic boron, transition-metal-doped borophene, monolayer monoxides and monochlorides of MgO and NaCl, MX_2 (M = Mo, W; X = S, Se), MXene and so on.[17–23]

The computational design of novel 2D materials has covered a wide range of s-, p- and d-block elements in the periodic table mainly through the bottom-up and/or global-minimum (GM) structure search approaches.[24–29] For example, the prediction of B_2C/Al_2C monolayers is inspired by the planar geometry and delocalized electronic structures in CB_4/$C_2Al_6^{2-}$ molecular building blocks through a bottom-up design process.[30–32] Luo *et al.* predicted graphene-like monolayer monoxides and monochlorides (*e.g.*, MgO and NaCl) based on their rock-salt-like bulks with space point group $Fm\bar{3}m$.[19] Besides, a GM structure search is another approach based on the development of relevant packages such as USPEX, CALYPSO, LASP, and TGMin.[33–36] By using the GM approach, a series of 2D materials, such as boron–carbon and Cu_2Si monolayer, are predicted to be stable both dynamically and thermodynamically.[37,38] Apart from that, Wang *et al.* predicted the Be_5C_2 monolayer by combining these two strategies.[39] All these computationally predicted 2D materials are composed of s- and p-block main-group elements as well as d-block transition metal elements,[17–19,40,41] whereas those composed of f-block elements (lanthanides and actinides) are relatively rare, with only a few examples such as the low-dimensional f-block element borides.[42,43]

Uranium is the heaviest abundant f-block actinide element available in natural environments and its most stable form is uranyl, which is the linear divalent cation UO_2^{2+} with significant stability.[44,45] Uranyl-based compounds, clusters, and 2D/3D materials[46–51] have sparked tremendous interest due to their fascinating topological structures and potential applications in the field of underground water, nuclear waste, and fuel reprocessing.[52–56] Among them, a variety of uranyl clusters experimentally synthesized by Burns and colleagues show similar topologies to carbon fullerene clusters such as C_{20} and C_{60}. For example, $[UO_2(O_2)(OH)]_{60}^{60-}$ (denoted as $[U_{60}]$ hereafter) is experimentally found to adopt the same topology as C_{60} buckyballs consisting of 12 pentagons and 20 hexagons shown in Scheme 1(a) and (c).[54,57–60] The topological similarity between the fullerene-like uranyl cluster $[U_{60}]$ and C_{60} prompts us to wonder whether the graphene-like 2D uranyl sheet as presented

[a]*Department of Chemistry and Key Laboratory of Organic Optoelectronics & Molecular Engineering of Ministry of Education, Tsinghua University, Beijing 100084, China. E-mail: hshu@mail.tsinghua.edu.cn*

[b]*Department of Chemistry, Southern University of Science and Technology, Shenzhen 518055, China*

† Dedicated to Professor Zhifang Chai on the occasion of his 80th birthday.

‡ Electronic supplementary information (ESI) available: Theoretical and computational details. See https://doi.org/10.1039/d2sc02017c

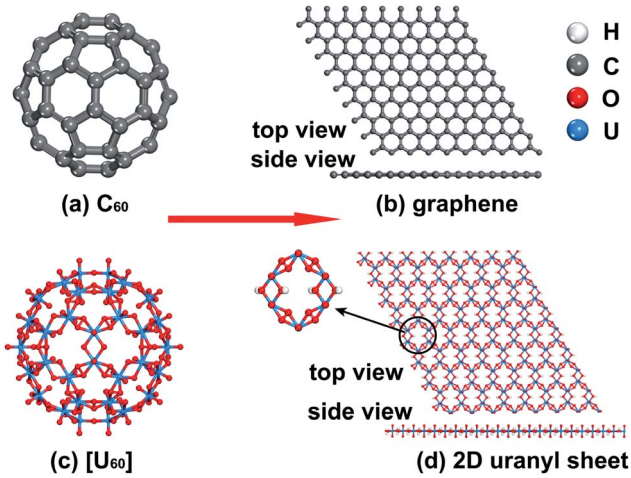

Scheme 1 An analogy between the geometries of carbon- and uranyl-based clusters and 2D sheets. (a) C_{60} fullerene cluster; (b) 2D graphene sheet; (c) fullerene-like $[U_{60}]$ cluster; (d) graphene-like 2D uranyl sheet and corresponding hexagonal uranyl-unit ring.

in Scheme 1(d) is stable or not. In this regard, it is worth noting that low-dimensional mineral materials of uranyl indeed exist, as exemplified by rutherfordine (UO_2CO_3) and studtite ($UO_2(O_2)(H_2O)_2$) discovered in the early 20th century.[61,62]

In this work, by combining both bottom-up and GM structure search strategies, a novel graphene-like 2D uranyl material is computationally predicted to be highly stable, thus extending the design of graphene-like 2D materials to the domain of f-block actinides that are stable kinetically and thermodynamically. Furthermore, the 2D uranyl sheet features a rare type of 1D spin-1/2 Heisenberg chain with a long-range antiferromagnetic (AFM) spin order on the superoxido groups,[63–66] where there exists a new type of $2p_{\pi^*}$–$5f_{\delta}$–$2p_{\pi^*}$ superexchange interaction. Most often, the AFM order in crystals is caused by the superexchange interaction among the d-type AOs of transition metals *via* the p-type AOs of the ligands.[67,68] Therefore, this antiferromagnetically coupled 1D spin-1/2 Heisenberg chain of p-orbital based superoxido centers with surrounding uranyl ions forms a new pillar in the field of f-block element low-dimensional spin systems.[69,70]

Results and discussion

The graphene-like 2D uranyl monolayer sheet is designed through the bottom-up approach inspired by the analogy of the uranyl nanocluster of $[U_{60}]$ with C_{60}, and thus the atomic composition is set as $(UO_2)_2(\mu_2\text{-}O_2)_2(\mu_2\text{-}OH)_2$ for further GM structure search. This selection of composition aims at circumventing formation of discrete small clusters in the presence of counterions. The evolutionary algorithm code USPEX for the GM search, which has been successfully used to predict a number of experimentally confirmed new materials, is applied to search for thermodynamically stable structures of a given fixed-composition system.[71–74] Based on the optimal structures found from USPEX, we performed relativistic quantum chemical calculations and *ab initio* molecular dynamics simulations using density functional theory. The recently developed Goedecker–Teter–Hutter (GTH) pseudopotential by Lu *et al.* was used to model the core electrons with 14 valence electrons for U.[75] Various chemical bonding analyses are applied to provide understanding of the stability and electronic structures. The computational details are given in the ESI.‡

Geometric structures of the 2D uranyl monolayer sheet

Through an extensive GM structure search with evolutionary algorithm USPEX, a planar hexagonal graphene-like 2D uranyl sheet has been located, as shown in Fig. 1(a), where the uranyl groups are connected by two superoxido groups and a pair of hydroxyl bridges. This structure is found to be 16 meV per atom lower in energy than the second-most stable one with a uranyl ribbon structure (Fig. 1(b)). The third-most stable one seen in Fig. 1(c) is a distorted hexagonal quasi-2D structure lying 33 meV per atom higher, in which the superoxido groups are slightly off the plane due to the steric effect. Comparatively, the fourth one in Fig. 1(d), 49 meV per atom higher in energy, tends to form a bulk 3D structure with hydrogen bonds rather than the 2D pattern. To verify the reliability of the DFT functional, we did further calculations by employing the HSE06 functional to determine the single point energies of these four most stable isomers and the calculated order is consistent with the results obtained from the PBE functional (Table S1‡). More isomers within the range of 320 meV per atom higher in energy are shown in Fig. S1.‡ In addition, this optimal structure has been further confirmed to be stable by phonon spectrum calculations along the high-symmetry lines in the Brillouin zone. As shown in Fig. S2,‡ there is no imaginary phonon mode in the phonon spectrum, suggesting the kinetic stability of this uranyl sheet.

The GM structure search and phonon spectrum suggest that the graphene-like 2D uranyl sheet is stable in terms of energy and kinetics. Our calculation shows that the computationally optimized 2D uranyl structure has maintained the planar graphene-like 2D topology, which is in line with the previous

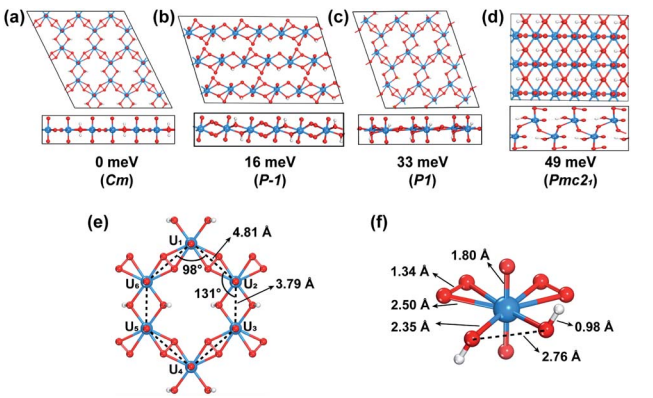

Fig. 1 (a–d) Top (upper) and side (lower) views of the four most stable structures from the GM structure search *via* the USPEX program. The relative energy per atom and corresponding space groups (in parentheses) are indicated. (e) The hexagonal uranyl-unit structure of the most stable 2D uranyl sheet, and (f) its corresponding coordination environment of the uranyl building block. Uranium, oxygen and hydrogen atoms are in blue, red and white, respectively.

quantum chemical calculations and experimental results of the molecular compound $K_6[(UO_2)(O_2)_2(OH)]_2(H_2O)_7$, where the U–$(OH)_2$–U structure is planar with a dihedral angle of 180°.[76–78] As shown in Fig. 1, our 2D sheet is composed of a honeycomb-like hexagonal unit with six uranyl ligands (Fig. 1(e)). The six U atoms in each unit form a hexagon with D_{2h} local symmetry, where the four neighboring U–U distances bridged by superoxido are 4.81 Å and the remaining two bridged by a pair of hydroxyl groups are 3.79 Å. Consequently, there are two kinds of interior angles of 98° and 131°, respectively. This distortion from ideal D_{6h} to D_{2h} local symmetry of the hexagonal ring is attributed to the two types of bridging ligands of superoxido and hydroxyl connecting the six uranyl groups altogether. All the U and O atoms from the bridging ligands form one planar 2D structure while the remaining O_{yl} atoms are perpendicularly connected with U with a rather short U–O bond length of 1.80 Å, which is almost the same as that in the naked uranyl complex. The H atoms are off the plane and the O–H bond length is 0.98 Å, close to that in water (0.97 Å). The U–$O_{superoxido}$ bond length is 2.50 Å, which is longer than that of U–$O_{hydroxyl}$ (2.35 Å). The O–O bond length of the superoxido ligand in the 2D uranyl sheet is 1.34 Å, close to that of the naked one (1.33 Å) as well as that of a recently reported uranyl superoxide compound (1.39 Å).[79]

The similarities between $[U_{60}]$ and C_{60} clusters as well as between graphene and the 2D uranyl sheet underscore the analogy between the sp^2-hybridized carbon atom and uranyl. Firstly, both of them prefer forming ligand connections on the equatorial plane since the axial direction is occupied by the perpendicular p_z AO of the sp^2-hybridized carbon atom or two rigid linear O_{yl} ligands in the linear uranyl cation of $[O{=}U{=}O]^{2+}$. Secondly, this analogy of the sp^2-hybridized carbon atom and uranyl has been further confirmed by using the π-orbital axis vector (POAV) method with pyramidalization angle as shown in Scheme 2.[80–82] For carbon atoms in the C_{60} cluster, the pyramidalization angle defined as $\theta_p = (\theta_{\sigma\pi} - 90^\circ) = 11.6^\circ$, where $\theta_{\sigma\pi}$ is the angle between the σ- and π-bonding orbitals (Scheme 2(a)), is almost equal to the angle of $\theta_p = (\theta_{O\text{–}U\text{–}U} - 90^\circ) = 12.6^\circ$ in the $[U_{60}]$ cluster, where $\theta_{O\text{–}U\text{–}U}$ is the angle between one O_{yl} atom and its connected U atom as well as the neighboring U atom bridged by the superoxido group (Scheme 2(b)). Comparatively, the $\theta_p = 0^\circ$ in graphene (Scheme 2(c)) is very close to the $\theta_p = 1.0^\circ$ based on an optimized 2D uranyl sheet (Scheme 2(d)), further showing the similarity between the sp^2-hybridized carbon atom and uranyl.

In order to better understand the geometric structure of this novel 2D uranyl sheet, we have also made a detailed geometry comparison between the experimentally synthesized $[U_{60}]$ cluster and this computationally predicted graphene-like 2D uranyl sheet. As shown in Table S2,‡ the U–O_{yl} bond length (1.80 Å) of uranyl in this 2D sheet is comparable to that in the $[U_{60}]$ cluster (1.76–1.84 Å). Besides, both the U–O_2–U and U–$(OH)_2$–U dihedral angles are planar (180.0°) in the 2D uranyl sheet, while the corresponding ones are within the range of 143.2–159.7° and 174.0–175.0° in the cluster, respectively. In contrast to the aforementioned 1.34 Å bond length of the O_2 moiety in the 2D uranyl sheet, the shortest O–O bond length of the peroxide in the $[U_{60}]$ cluster is 1.46 Å, which is in agreement with the bond length in the naked peroxide group (1.49 Å). The O–O bond length difference between the 2D uranyl sheet and $[U_{60}]$ cluster likely arises from the fact that the O_2 moiety in the 2D uranyl sheet is indeed a superoxide (O_2^-), rather than the typical peroxide group (O_2^{2-}) in the uranyl clusters.

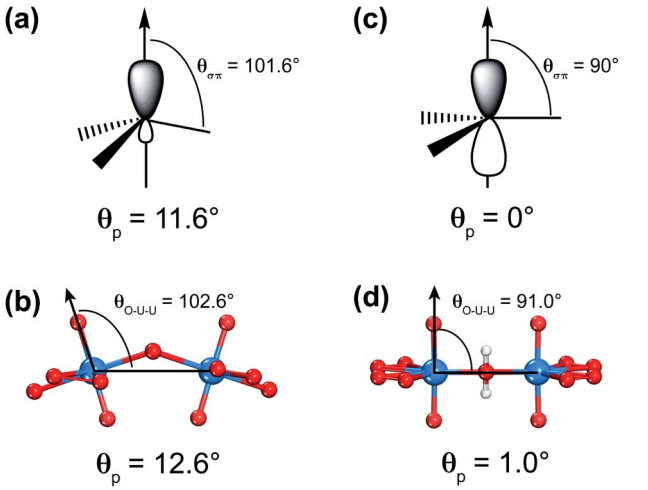

Scheme 2 An analogy between the sp^2-hybridized carbon atom and uranyl. The sp^2-hybrid orbital and pyramidalization angle (θ_p) of carbon in (a) C_{60} buckyball fullerene and (c) graphene. The $[U_2]$ fragment with bent uranyl-hydroxyl/superoxido bridges and corresponding θ_p of uranyl in (b) the fullerene-like $[U_{60}]$ cluster and (d) graphene-like 2D uranyl sheet.

Thermodynamic and thermal stabilities of the 2D uranyl sheet

To investigate the thermodynamics of the 2D uranyl sheet, we have computed the formation energies from the reactants available in nature (H_2O, O_2 and solid UO_2) and the proposed reaction is shown in eqn (1). The formation free energy (ΔG_{300K}) at a temperature of 300 K was calculated using the formula $\Delta G_{300K} = G((UO_2)_4(\mu_2\text{-}O_2)_4(\mu_2\text{-}OH)_4) - 4G(UO_2) - 2G(H_2O) - 5G(O_2)$, where $G(UO_2)$ is the energy of the uranium dioxide crystal with the entropy and zero-point energies corrected. The calculated ΔG_{300K} is negative, with a value of −41.3 kcal mol^{-1}, indicating that the formation of the 2D uranyl sheet is energetically favorable under these conditions.

$$2H_2O + 5O_2 + 4UO_2 \rightarrow (UO_2)_4(\mu_2\text{-}O_2)_4(\mu_2\text{-}OH)_4,\ \Delta G_{300K} = -41.3\ \text{kcal mol}^{-1} \quad (1)$$

In order to examine the thermal stability of the predicted uranyl sheet, a series of spin-polarized AIMD simulations were carried out at various temperatures of 300 K, 400 K, 500 K, and 600 K for durations of 10 ps, respectively, and 5 ps for the simulations at 1000 K because the structure starts to collapse. Snapshots with top and side views taken at the end of each simulation are shown in Fig. 2(a). The hexagonal framework of the uranyl sheet is well-maintained at the temperature of 300 K after 10 ps simulations, indicating that it is stable at room temperature. As expected, at the relatively high temperature of 500 K, it shows a little more disordering while there is much

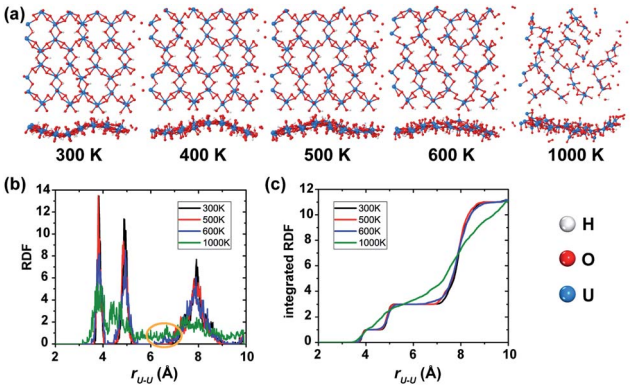

Fig. 2 (a) The snapshots of the final frame of each spin-polarized AIMD simulation from 300 K to 1000 K (top and side views). (b) The radial distribution function (RDF) and (c) corresponding integrated RDF of U–U bond lengths at different temperatures for the spin-polarized calculation.

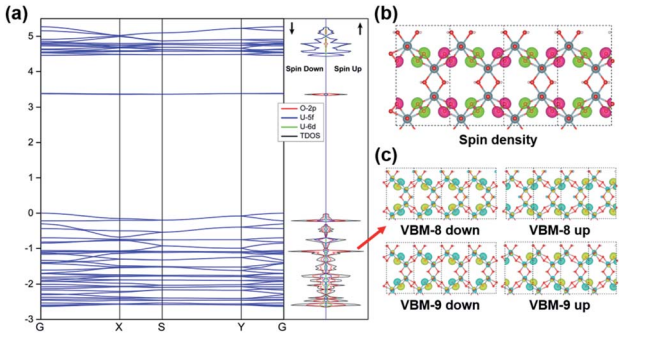

Fig. 3 (a) Band structure and partial density of states (DOS) of the 2D uranyl sheet. The Fermi level is assigned at 0 eV. The four points of *G* (0, 0, 0), *X* (0.5, 0, 0), *S* (0.5, 0.5, 0) and *Y* (0, 0.5, 0) refer to the high-symmetry points of the first Brillouin zone in reciprocal space. (b) The spin density of the 2D uranyl sheet for the AFM ground state. The isovalue is 0.002 e Å^{-3}. (c) The $2p_{\pi^*}$ singly occupied real space wavefunctions for the four corresponding bands at the gamma point. All the results are based on the calculation at the HSE06 hybrid functional level.

more disordering at 600 K. At the temperature of 1000 K, the monolayer structure breaks down rapidly even in 5 ps. Since uranyl is the backbone of the material, the radial distribution function (RDF) of the neighboring U–U distances is a good parameter for quantitatively evaluating the structure deformation of the sheet during the AIMD simulations at different temperatures. As shown in Fig. 2(b), the RDF in the range of 6–7 Å starts to have noise at 600 K which becomes larger at 1000 K, while it remains at zero at 300 K and 500 K. It follows that the uranyl sheet begins to reconstruct at the temperature of 600 K and collapses at 1000 K. Furthermore, there are no obvious steps in the integrated RDF at 1000 K (shown in Fig. 2(c)), indicating the it has become completely disordered within 5 ps. Fluctuations of the total potential energy for the sheet at different temperatures during AIMD simulations (see Fig. S3‡) also confirm that it is relatively thermally stable up to 500 K. When the temperature goes higher such as between 600 K and 1000 K, the sheet has enough kinetic energy to cross the barrier and tends to decompose. Meanwhile, similar non-spin-polarized AIMD simulations were also carried out at temperatures of 100 K, 300 K, 400 K, 500 K, and 1000 K for durations of 10 ps, 10 ps, 10 ps, 10 ps, and 4 ps, respectively for comparison. Both the corresponding snapshots (Fig. S4‡) and RDF (Fig. S5‡) analysis show that the reconstruction of the non-spin-polarized 2D uranyl sheet happens at merely 400 K compared to the aforementioned distortion temperature of 600 K for the spin-polarized calculation. The relatively more stable structure in the spin-polarized state indicates that the AFM coupling interactions may contribute to the stability of the uranyl sheet when compared with the non-magnetic sheet.

Electronic structures and stabilization mechanism in the graphene-like 2D uranyl sheet

The stability of the 2D graphene-like uranyl sheet is dependent on the electronic structures as well as the thermodynamic conditions. The electronic structure and related properties of the uranyl sheet are revealed by the calculated band structure, density-of-states (DOS), spin densities, and real space wavefunctions at the gamma point, as displayed in Fig. 3. The 2D uranyl sheet turns out to be a semiconductor with an approximate 3.4 eV energy gap at the HSE06 hybrid functional level. The flat band above the Fermi level in Fig. 3(a) can be attributed to the out-of-plane $2p_{\pi^*}$ orbitals of the superoxido groups and the corresponding charge density of the conduction band minimum (CBM) (see in Fig. S7‡). Meanwhile, the valence band maximum (VBM) shows some π-type bonding interaction between the in-plane $2p_{\pi^*}$ orbitals in the superoxido groups and 5f/6d orbitals of the uranium atoms.

Additionally, more bonding interactions in this 2D uranyl sheet are revealed by the inner nine real space wavefunctions shown in Fig. S8,‡ among which there are the π-type (*i.e.*, VBM-2, VBM-3, and VBM-14) and σ-type (*i.e.*, VBM-4, VBM-5, VBM-10, VBM-12, VBM-13, and VMB-17) bonding interactions contributing to stabilizing this uranyl sheet. The above-mentioned σ/π bonding interactions are mainly contributed by O-2p and U-5f/6d AOs which can be revealed by the partial DOS analysis in Fig. 3(a). As U 5f orbitals are energetically close to O 2p ones while 6d orbitals are radially more extended, they both interact with the O_2^- species significantly. From the DFT optimized results, the 2D uranyl sheet has an AFM singlet ground state which is more stable than the ferromagnetic (FM) state by 4.3 meV per atom. Moreover, the AFM ground state is also confirmed by the spin densities located on the superoxido groups as shown in Fig. 3(b), where each group has a spin density of 0.81 with spin up (green) or spin down (pink), respectively. Meanwhile, Fig. 3(c) shows the real space wavefunction VBM-8 and VBM-9 corresponding to singly occupied $2p_{\pi^*}$ electrons of the superoxido groups, indicating the AFM order in the 2D uranyl sheet as well.

$$H = -J\sum_{i<j}\vec{S}_i\cdot\vec{S}_j + H_0 \quad (2)$$

To further study the novel magnetic behavior in the 2D uranyl sheet, the Heisenberg model (see eqn (2)) and three

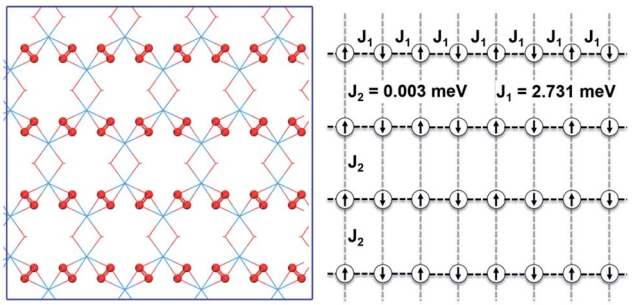

Fig. 4 The structure of the graphene-like 2D uranyl sheet (left) and schematic presentation of the 1D antiferromagnetic chains (right) derived from the singly occupied $2p_{\pi^*}$ electrons of the superoxido groups. The path for the 1D antiferromagnetic interaction is indicated by the black dashed lines. J_1 and J_2 are the intra- and inter-chain coupling constants, respectively. O and U atoms are in red and blue, respectively.

different magnetic states with ferromagnetic (FM), antiferromagnetic (AFM), and antiferromagnetic/ferromagnetic (AF/FM) coupling (see in Fig. S9‡) were applied to calculate the intra-chain (J_1) and inter-chain (J_2) exchange coupling constants of this 2D material. In eqn (2), J is the exchange coupling constant, H_0 is the nonmagnetic Hamiltonian, and $\vec{S}_i$ and $\vec{S}_j$ are the spin momenta at sites i and j, respectively. As shown in Fig. 4, the simulated exchange coupling constant J_1 is 2.731 meV (22.03 cm^{-1}) and J_2 is 0.003 meV (0.024 cm^{-1}). Due to the relatively small interchain exchange coupling ($J_2 \ll J_1$), the 2D uranyl sheet shows a novel type of long-range 1D spin-1/2 Heisenberg chains with the superexchange interaction between the AFM p-type spin on each superoxido group, owing to unpaired $2p_{\pi^*}$ electrons on the superoxido groups *via* the empty $5f_\delta$ orbitals of the uranyl ligands. As shown in Scheme 3, the $5f_\delta$ orbital of the uranyl center and adjacent superoxido $2p_{\pi^*}$ orbitals are symmetry matching, thus providing a possible pathway for the superexchange interaction. For the case of the AFM state, the unpaired $2p_{\pi^*}$ electrons on the neighboring superoxido groups have opposite spins. One $2p_{\pi^*}$ electrons can hop directly to the nearby site *via* an intermediate $5f_\delta$ orbital of the uranyl due to the adaptable symmetry. This hopping reduces the kinetic energy of the electrons and stabilizes the 2D uranyl sheet. In contrast, for the case of the FM state, the neighboring unpaired $2p_{\pi^*}$ electrons have parallel spins. Thus, direct hopping is forbidden in the FM state, as the intermediate

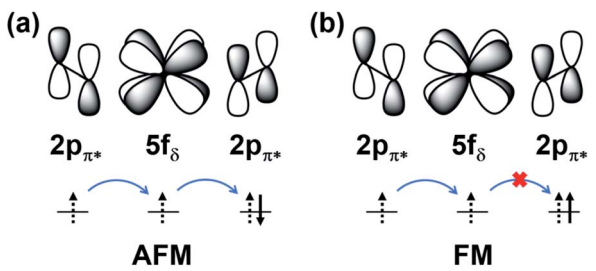

Scheme 3 The schematic illustration of $2p_{\pi^*}$–$5f_\delta$–$2p_{\pi^*}$ superexchange interactions of AFM (a) and FM (b) states.

state with two electrons on the same orbital of same spin would violate the Pauli exclusion principle. The possible $2p_{\pi^*}$–$5f_\delta$–$2p_{\pi^*}$ superexchange interactions help explain the AFM ground state of the 2D uranyl sheet. As quantum antiferromagnets like the one-dimensional Heisenberg antiferromagnetic chain of $S = 1/2$ spins (1D-HAF) are the ground for finding new states of matter and testing magnetic theoretical models, our system achieves the first inorganic p-orbital 1D-HAF with f-block elements. In all known 1D-HAFs, the spin states arise from the electrons in the d orbitals of transition-metal ions, except in the recently found CsO_2;[83] our system thus provides a new p-orbital 1D-HAF with f-block elements. Furthermore, the p-orbital antiferromagnetism with weak spin–orbit interaction can also be characterized by the small magnetic anisotropy energy (MAE) value of 0.06 meV per superoxido group obtained *via* the calculated energies with seven types of different spin orientations shown in Table S5‡.[84]

The stabilizing mechanism of this novel 2D uranyl sheet can be further analyzed on the basis of cluster models containing two/six uranyl ligands from the 2D sheet through the principal interacting orbital (PIO) and energy decomposition analysis with natural orbitals for chemical valence (EDA-NOCV) approaches.[85–88] Herein, we adopt the dimer molecular models of $(UO_2)_2(\mu_2\text{-}O_2)(O_2)_2(OH)_4^{3-}$ and $(UO_2)_2(O_2)_4(\mu_2\text{-}OH)_2^{2-}$ anions for the PIO analysis and the hexagonal ring model of the $(UO_2)_6(\mu_2\text{-}O_2)_4(\mu_2\text{-}OH)_4^{4+}$ cluster for the EDA-NOCV analysis. The corresponding EDA-NOCV results for the interactions between the superoxido groups $(\mu_2\text{-}O_2)_4^{4-}$ and uranyl fragment $(UO_2)_6(\mu_2\text{-}OH)_4^{8+}$ are listed in Table S6.‡ The calculated electrostatic interaction reaches up to -2734.64 kcal mol^{-1}. The orbital interaction (ΔE_{orb}) is divided into two major terms, $\Delta E_{orb(\pi)}$ and $\Delta E_{orb(\sigma)}$, with energies of -218.35 and -67.76 kcal mol^{-1}, respectively. The σ- & π-types of interactions are revealed by the π-type (PIMO 1) and σ-type (PIMO 4) bonding interactions from PIO analysis (Fig. S11‡). As for the bonding interactions between the fragments of $(\mu_2\text{-}OH)_4^{4-}$ and $(UO_2)_6(\mu_2\text{-}O_2)_4^{8+}$, Table S7‡ shows that the orbital interaction energies of $\Delta E_{orb(\pi)}$ and $\Delta E_{orb(\sigma)}$ are -252.55 and -143.30 kcal mol^{-1}, respectively. Overall, the results show that the σ/π bonding interactions and the electrostatic attraction between the superoxido/hydroxyl ligands and the uranyl cations play an important role in stabilizing the 2D hexagonal structure, which account for the special stability of the 2D uranyl sheet. Besides, based on the O–O bond length (1.34 Å) mentioned above, the O_2 moiety in the 2D uranyl sheet is a superoxide group with a singly occupied electron on each moiety. This assignment has further been supported by the electronic structure analysis of a hexagonal uranyl model cluster. As shown in Fig. S14,‡ there are twelve electrons occupied on the $2p_{\pi^*}$ orbitals of the four superoxido moieties in the cluster, where each superoxido has three occupied $2p_{\pi^*}$ electrons with the spin density close to 1, similar to other superoxides.

Conclusions

In summary, an unexpected graphene-like 2D uranyl material has been designed and predicted by the combination of both bottom-up and GM structure search strategies. This planar

sheet has a geometry similar to that of graphene with a honeycomb-like hexagonal unit of six uranyl ligands and each of the uranyl groups are bridged by superoxido/hydroxyl moieties. The superoxido bridges are calculated to possess one unpaired $2p_{\pi^*}$ electron each and are antiferromagnetically coupled with each other through the uranyl center. The rather small inter-chain exchange coupling constant ($J_2 = 0.003$ meV) and much larger intra-chain exchange coupling constant ($J_1 = 2.731$ meV) lead to a 1D spin-1/2 Heisenberg chain on superoxido groups. It forms a unique type of $2p_{\pi^*}$–$5f_{\delta}$–$2p_{\pi^*}$ superexchange pathway across the two neighboring superoxido groups *via* the uranyl. Especially noteworthy is the novel occurrence of p-orbital antiferromagnetism with this new material. A computational investigation shows that this 2D f-block actinide material has thermodynamic, kinetic and thermal stabilities, suggesting it is likely to be synthesized experimentally under a suitable environment. Our study extends the design of graphene-like 2D materials to f-block actinide elements, and helps to enrich the diversity and potential applications of 2D materials in p-orbital antiferromagnetic spintronics.

Data availability

The data that supports the findings of this study is available from the corresponding author upon reasonable request.

Author contributions

H. S. H. designed the project. X. K. Z. performed GM structure search, relativistic quantum chemical calculations and *ab initio* molecular dynamics simulations. C. S. C. and J. C. L. help to analyse the details and results of density functional theory calculations. J. B. L. provided the GTH pseudopotential basis of uranium. X. K. Z., H. S. H., and J. L. wrote and edited the manuscript.

Conflicts of interest

There are no conflicts to declare.

Acknowledgements

The authors are grateful to Professors Xiaojun Wu from the University of Science and Technology of China and Yong Xu and Hai Xiao from Tsinghua University for helpful discussions. This work was financially supported by the National Natural Science Foundation of China (Grant No. 21906094, 22076095, and 22033005) and Guangdong Provincial Key Laboratory of Catalysis (No. 2020B121201002). The calculations were performed using supercomputers at SUSTech Supercomputer Center and Tsinghua National Laboratory for Information Science and Technology. The Tsinghua Xuetang Talents Program is acknowledged for providing computational resources.

References

1 D. Basko, *Science*, 2011, **334**, 610–611.
2 A. J. Mannix, X.-F. Zhou, B. Kiraly, J. D. Wood, D. Alducin, B. D. Myers, X. Liu, B. L. Fisher, U. Santiago and J. R. Guest, *Science*, 2015, **350**, 1513–1516.
3 F. Shahzad, M. Alhabeb, C. B. Hatter, B. Anasori, S. M. Hong, C. M. Koo and Y. Gogotsi, *Science*, 2016, **353**, 1137–1140.
4 Z. Du, S. Yang, S. Li, J. Lou, S. Zhang, S. Wang, B. Li, Y. Gong, L. Song and X. Zou, *Nature*, 2020, **577**, 492–496.
5 M. Zeng, Y. Chen, E. Zhang, J. Li, R. G. Mendes, X. Sang, S. Luo, W. Ming, Y. Fu, M.-H. Du, L. Zhang, D. S. Parker, R. R. Unocic, K. Xiao, C. Wang, T. Zhang, Y. Xiao, M. H. Rümmeli, F. Xiu and L. Fu, *CCS Chem.*, 2019, **1**, 117–127.
6 Q.-Q. Huang, Y.-Z. Li, Z. Zheng, X.-M. Jiang, S.-S. Sun, H.-J. Jiang, W.-H. Deng, G.-E. Wang, T.-Y. Zhai, M.-D. Li and G. Xu, *CCS Chem.*, 2020, **2**, 655–662.
7 W. Zeng and J. Wu, *Chem*, 2021, **7**, 358–386.
8 X. Liu, Z. Yang, C. Ge, H. Li, M. Hao, C. Wan, Y. Song, B. Li and Q. Dong, *CCS Chem.*, 2021, **3**, 2576–2583.
9 S. Tao and D. Jiang, *CCS Chem.*, 2021, **3**, 2003–2024.
10 J. Wang, P. Yang, L. Liu, B. Zheng, J. Jiang, J.-p. Ma, Y. Yan, S. Yang, L. Yang, Q.-K. Liu, Y. Han and Y. Chen, *CCS Chem.*, 2021, **3**, 2372–2381.
11 Q. Pan, S. Chen, C. Wu, F. Shao, J. Sun, L. Sun, Z. Zhang, Y. Man, Z. Li, L. He and Y. Zhao, *CCS Chem.*, 2021, **3**, 1368–1375.
12 C. Liu, Y. Wang, H. Li, Y. Wu, Y. Li, J. Li, K. He, Y. Xu, J. Zhang and Y. Wang, *Nat. Mater.*, 2020, **19**, 522–527.
13 K. S. Novoselov, A. K. Geim, S. V. Morozov, D. Jiang, Y. Zhang, S. V. Dubonos, I. V. Grigorieva and A. A. Firsov, *Science*, 2004, **306**, 666–669.
14 C. Lee, X. Wei, J. W. Kysar and J. Hone, *Science*, 2008, **321**, 385–388.
15 R. R. Nair, P. Blake, A. N. Grigorenko, K. S. Novoselov, T. J. Booth, T. Stauber, N. M. Peres and A. K. Geim, *Science*, 2008, **320**, 1308.
16 Y. Cao, V. Fatemi, S. Fang, K. Watanabe, T. Taniguchi, E. Kaxiras and P. Jarillo-Herrero, *Nature*, 2018, **556**, 43–50.
17 F. Ma, Y. Jiao, G. Gao, Y. Gu, A. Bilic, Z. Chen and A. Du, *Nano Lett.*, 2016, **16**, 3022–3028.
18 H. Zhang, Y. Li, J. Hou, K. Tu and Z. Chen, *J. Am. Chem. Soc.*, 2016, **138**, 5644–5651.
19 B. Luo, Y. Yao, E. Tian, H. Song, X. Wang, G. Li, K. Xi, B. Li, H. Song and L. Li, *Proc. Natl. Acad. Sci. U. S. A.*, 2019, **116**, 17213–17218.
20 H. S. S. Ramakrishna Matte, A. Gomathi, A. K. Manna, D. J. Late, R. Datta, S. K. Pati and C. N. R. Rao, *Angew. Chem., Int. Ed.*, 2010, **49**, 4059–4062.
21 M. Barsoum, J. Golczewski, H. Seifert and F. Aldinger, *J. Alloys Compd.*, 2002, **340**, 173–179.
22 L. Ding, Y. Wei, Y. Wang, H. Chen, J. Caro and H. Wang, *Angew. Chem., Int. Ed.*, 2017, **56**, 1825–1829.
23 S. Zhang, Z. Yan, Y. Li, Z. Chen and H. Zeng, *Angew. Chem., Int. Ed.*, 2015, **54**, 3112–3115.
24 P. D. Pancharatna, M. A. Méndez-Rojas, G. Merino, A. Vela and R. Hoffmann, *J. Am. Chem. Soc.*, 2004, **126**, 15309–15315.
25 Y. Wang, Y. Li and Z. Chen, *J. Mater. Chem. C*, 2015, **3**, 9603–9608.

26 L.-M. Yang, E. Ganz, Z. Chen, Z.-X. Wang and P. v. R. Schleyer, *Angew. Chem., Int. Ed.*, 2015, **54**, 9468–9501.
27 W.-L. Li, X. Chen, T. Jian, T.-T. Chen, J. Li and L.-S. Wang, *Nat. Rev. Chem.*, 2017, **1**, 0071.
28 Y. Wang, Y. Li and Z. Chen, *Acc. Chem. Res.*, 2020, **53**, 887–895.
29 D. Wu, H. Lv, Z. Zhuo, X. Li, X. Wu and J. Yang, *J. Phys. Chem. Lett.*, 2021, **12**, 3528–3534.
30 Y. Li, Y. Liao, P. von Ragué Schleyer and Z. Chen, *Nanoscale*, 2014, **6**, 10784–10791.
31 J. Dai, X. Wu, J. Yang and X. C. Zeng, *J. Phys. Chem. Lett.*, 2014, **5**, 2058–2065.
32 X. Wu, Y. Pei and X. C. Zeng, *Nano Lett.*, 2009, **9**, 1577–1582.
33 Y. Wang, J. Lv, L. Zhu and Y. Ma, *Comput. Phys. Commun.*, 2012, **183**, 2063–2070.
34 C. W. Glass, A. R. Oganov and N. Hansen, *Comput. Phys. Commun.*, 2006, **175**, 713–720.
35 S. D. Huang, C. Shang, P. L. Kang, X. J. Zhang and Z. P. Liu, *Wiley Interdiscip. Rev.: Comput. Mol. Sci.*, 2019, **9**, e1415.
36 X. Chen, Y. F. Zhao, Y. Y. Zhang and J. Li, *J. Comput. Chem.*, 2019, **40**, 1105–1112.
37 X. Luo, J. Yang, H. Liu, X. Wu, Y. Wang, Y. Ma, S.-H. Wei, X. Gong and H. Xiang, *J. Am. Chem. Soc.*, 2011, **133**, 16285–16290.
38 L.-M. Yang, V. Bacic, I. A. Popov, A. I. Boldyrev, T. Heine, T. Frauenheim and E. Ganz, *J. Am. Chem. Soc.*, 2015, **137**, 2757–2762.
39 Y. Wang, F. Li, Y. Li and Z. Chen, *Nat. Commun.*, 2016, **7**, 11488.
40 H. Zhang, Y. Li, J. Hou, A. Du and Z. Chen, *Nano Lett.*, 2016, **16**, 6124–6129.
41 Y. Jiao, F. Ma, J. Bell, A. Bilic and A. Du, *Angew. Chem., Int. Ed.*, 2016, **55**, 10292–10295.
42 A. Lopez-Bezanilla, *J. Phys.: Mater.*, 2020, **3**, 024002.
43 A. Lopez-Bezanilla, *Phys. Rev. Mater.*, 2021, **5**, 034007.
44 J. Qiu and P. C. Burns, *Chem. Rev.*, 2013, **113**, 1097–1120.
45 B. E. Cowie, J. M. Purkis, J. Austin, J. B. Love and P. L. Arnold, *Chem. Rev.*, 2019, **119**, 10595–10637.
46 P. Wei, N. Pu, X. Dong, J. Yuan, Y. Li, L. Xu, J. Chen and C. Xu, *Inorg. Chem.*, 2019, **58**, 11664–11671.
47 Y. Hao, P. Kegler, T. E. Albrecht-Schmitt, S. Wang, Q. Dong and E. V. Alekseev, *Eur. J. Inorg. Chem.*, 2020, **4**, 407–416.
48 L. Mei, P. Ren, Q. Y. Wu, Y. B. Ke, J. S. Geng, K. Liu, X. Q. Xing, Z. W. Huang, K. Q. Hu, Y. L. Liu, L. Y. Yuan, G. Mo, Z. H. Wu, J. K. Gibson, Z. F. Chai and W. Q. Shi, *J. Am. Chem. Soc.*, 2020, **142**, 16538–16545.
49 L. Wang, Z. Li, Q. Wu, Z. Huang, L. Yuan, Z. Chai and W. Shi, *Environ. Sci.: Nano*, 2020, **7**, 724–752.
50 J. Xie, Y. Wang, W. Liu, C. Liang, Y. Zhang, L. Chen, D. Sheng, Z. Chai and S. Wang, *Sci. China: Chem.*, 2020, **63**, 1608–1612.
51 H. Hu, X. Xu, C. Xu and J. Li, *Chin. J. Struct. Chem.*, 2020, **39**, 1201–1212.
52 K.-A. Hughes Kubatko, K. B. Helean, A. Navrotsky and P. C. Burns, *Science*, 2003, **302**, 1191–1193.
53 P. C. Burns, K. A. Kubatko, G. Sigmon, B. J. Fryer, J. E. Gagnon, M. R. Antonio and L. Soderholm, *Angew. Chem., Int. Ed.*, 2005, **44**, 2135–2139.
54 P. Miro and C. Bo, *Inorg. Chem.*, 2012, **51**, 3840–3845.
55 L. Zhang, M. Dembowski, A. Arteaga, S. Hickam, N. P. Martin, L. N. Zakharov, M. Nyman and P. C. Burns, *Inorg. Chem.*, 2019, **58**, 439–445.
56 C. R. Armstrong, M. Nyman, T. Shvareva, G. E. Sigmon, P. C. Burns and A. Navrotsky, *Proc. Natl. Acad. Sci. U. S. A.*, 2012, **109**, 1874–1877.
57 T. Z. Forbes, J. G. McAlpin, R. Murphy and P. C. Burns, *Angew. Chem., Int. Ed.*, 2008, **47**, 2824–2827.
58 G. E. Sigmon, D. K. Unruh, J. Ling, B. Weaver, M. Ward, L. Pressprich, A. Simonetti and P. C. Burns, *Angew. Chem., Int. Ed.*, 2009, **48**, 2737–2740.
59 G. E. Sigmon, J. Ling, D. K. Unruh, L. Moore-Shay, M. Ward, B. Weaver and P. C. Burns, *J. Am. Chem. Soc.*, 2009, **131**, 16648–16649.
60 V. Parasuk and J. Almlöf, *Chem. Phys. Lett.*, 1991, **184**, 187–190.
61 C. L. Christ, J. R. Clark and H. T. Evans, *Science*, 1955, **121**, 472–473.
62 P. C. Burns and K.-A. Hughes, *Am. Mineral.*, 2003, **88**, 1165–1168.
63 J. Kohler, *Angew. Chem., Int. Ed.*, 2010, **49**, 3114–3115.
64 D. Hirobe, M. Sato, T. Kawamata, Y. Shiomi, K.-i. Uchida, R. Iguchi, Y. Koike, S. Maekawa and E. Saitoh, *Nat. Phys.*, 2016, **13**, 30–34.
65 O. Breunig, M. Garst, A. Klümper, J. Rohrkamp, M. M. Turnbull and T. Lorenz, *Sci. Adv.*, 2017, **3**, eaao3773.
66 C. Wang, R. Sun, Y. Chen, B.-W. Wang, Z.-M. Wang and S. Gao, *CCS Chem.*, 2020, **2**, 362–368.
67 O. Domanov, E. Weschke, T. Saito, H. Peterlik, T. Pichler, M. Eisterer and H. Shiozawa, *Nanoscale*, 2019, **11**, 10615–10621.
68 A. Bonanni and T. Dietl, *Chem. Soc. Rev.*, 2010, **39**, 528–539.
69 J. L. Manson, K. H. Stone, H. I. Southerland, T. Lancaster, A. J. Steele, S. J. Blundell, F. L. Pratt, P. J. Baker, R. D. McDonald, P. Sengupta, J. Singleton, P. A. Goddard, C. Lee, M.-H. Whangbo, M. M. Warter, C. H. Mielke and P. W. Stephens, *J. Am. Chem. Soc.*, 2009, **131**, 4590–4591.
70 J. Zhang, L. Duan, Z. Wang, X. Wang, J. Zhao, M. Jin, W. Li, C. Zhang, L. Cao, Z. Deng, Z. Hu, S. Agrestini, M. Valvidares, H. J. Lin, C. T. Chen, J. Zhu and C. Jin, *Inorg. Chem.*, 2020, **59**, 5377–5385.
71 N. P. Salke, M. M. Davari Esfahani, Y. Zhang, I. A. Kruglov, J. Zhou, Y. Wang, E. Greenberg, V. B. Prakapenka, J. Liu, A. R. Oganov and J.-F. Lin, *Nat. Commun.*, 2019, **10**, 4453.
72 D. Zhou, D. V. Semenok, H. Xie, X. Huang, D. Duan, A. Aperis, P. M. Oppeneer, M. Galasso, A. I. Kartsev, A. G. Kvashnin, A. R. Oganov and T. Cui, *J. Am. Chem. Soc.*, 2020, **142**, 2803–2811.
73 A. R. Oganov, A. O. Lyakhov and M. Valle, *Acc. Chem. Res.*, 2011, **44**, 227–237.
74 A. O. Lyakhov, A. R. Oganov, H. T. Stokes and Q. Zhu, *Comput. Phys. Commun.*, 2013, **184**, 1172–1182.

75 J.-B. Lu, D. C. Cantu, C.-Q. Xu, M.-T. Nguyen, H.-S. Hu, V.-A. Glezakou, R. Rousseau and J. Li, *J. Chem. Theory Comput.*, 2021, **17**, 3360–3371.
76 B. Vlaisavljevich, L. Gagliardi and P. C. Burns, *J. Am. Chem. Soc.*, 2010, **132**, 14503–14508.
77 A. Arteaga, D. Ray, E. Glass, N. P. Martin, L. N. Zakharov, L. Gagliardi and M. Nyman, *Inorg. Chem.*, 2020, **59**, 1633–1641.
78 K.-A. Kubatko, T. Z. Forbes, A. L. Klingensmith and P. C. Burns, *Inorg. Chem.*, 2007, **46**, 3657–3662.
79 D. V. Kravchuk, N. N. Dahlen, S. J. Kruse, C. D. Malliakas, P. M. Shand and T. Z. Forbes, *Angew. Chem., Int. Ed.*, 2021, **60**, 15041–15048.
80 R. C. Haddon, *J. Am. Chem. Soc.*, 1987, **109**, 1676–1685.
81 R. C. Haddon, *Science*, 1993, **261**, 1545–1550.
82 X. Lu and Z. Chen, *Chem. Rev.*, 2005, **105**, 3643–3696.
83 T. Knaflič, M. Klanjšek, A. Sans, P. Adler, M. Jansen, C. Felser and D. Arčon, *Phys. Rev. B*, 2015, **91**, 174419.
84 A. Lehnert, S. Dennler, P. Błoński, S. Rusponi, M. Etzkorn, G. Moulas, P. Bencok, P. Gambardella, H. Brune and J. Hafner, *Phys. Rev. B*, 2010, **82**, 094409.
85 J.-X. Zhang, F. K. Sheong and Z. Lin, *Chem.–Eur. J.*, 2018, **24**, 9639–9650.
86 J.-X. Zhang, F. K. Sheong and Z. Lin, *Wiley Interdiscip. Rev.: Comput. Mol. Sci.*, 2020, **10**, e1469.
87 F. K. Sheong, J.-X. Zhang and Z. Lin, *Phys. Chem. Chem. Phys.*, 2020, **22**, 10076–10086.
88 M. P. Mitoraj, A. Michalak and T. Ziegler, *J. Chem. Theory Comput.*, 2009, **5**, 962–975.